Multiple Folding Pathways for the P4−P6 RNA Domain†

Scott K. Silverman,*,‡ Michael L. Deras,§ Sarah A. Woodson,§ Stephen A. Scaringe,|| and Thomas R. Cech*,‡,⊥

Department of Chemistry and Biochemistry and Howard Hughes Medical Institute, University of Colorado at Boulder, Boulder, Colorado 80309, Department of Biophysics, Johns Hopkins University, Baltimore, Maryland 21218, and Dharmacon Research, Inc., 3200 Valmont Road #5, Boulder, Colorado 80301

Received April 12, 2000; Revised Manuscript Received June 23, 2000

ABSTRACT: We recently described site-specific pyrene labeling of RNA to monitor Mg^{2+}-dependent equilibrium formation of tertiary structure. Here we extend these studies to follow the folding kinetics of the 160-nucleotide P4−P6 domain of the *Tetrahymena* group I intron RNA, using stopped-flow fluorescence with ∼1 ms time resolution. Pyrene-labeled P4−P6 was prepared using a new phosphoramidite that allows high-yield automated synthesis of oligoribonucleotides with pyrene incorporated at a specific 2′-amino-2′-deoxyuridine residue. P4−P6 forms its higher-order tertiary structure rapidly, with $k_{obs} = 15-31\ s^{-1}$ ($t_{1/2} \approx 20-50$ ms) at 35 °C and $[Mg^{2+}] \approx 10$ mM in Tris−borate (TB) buffer. The folding rate increases strongly with temperature from 4 to 45 °C, demonstrating a large activation enthalpy $\Delta H^{\ddagger} \approx 26$ kcal/mol; the activation entropy $\Delta S^{\ddagger}$ is large and positive. In low ionic strength 10 mM sodium cacodylate buffer at 35 °C, a slow ($t_{1/2} \approx 1$ s) folding component is also observed. The folding kinetics are both ionic strength- and temperature-dependent; the slow phase vanishes upon increasing $[Na^+]$ in the cacodylate buffer, and the kinetics switch completely from fast at 30 °C to slow at 40 °C. Using synchrotron hydroxyl radical footprinting, we confirm that fluorescence monitors the same kinetic events as hydroxyl radical cleavage, and we show that the previously reported slow P4−P6 folding kinetics apply only to low ionic strength conditions. One model to explain the fast and slow folding kinetics postulates that some tertiary interactions are present even without Mg^{2+} in the initial state. The fast kinetic phase reflects folding that is facilitated by these interactions, whereas the slow kinetics are observed when these interactions are disrupted at lower ionic strength and higher temperature.

Early investigations of transfer RNAs revealed the existence of RNA tertiary structure, which usually forms after assembly of secondary structure elements such as stems and loops (*1*−*3*). Several crystal structures of tRNAs revealed the details of tertiary interactions in these molecules (*4*−*8*). Since then, the structures of several folded RNAs have been determined by X-ray crystallography or NMR spectroscopy (for example, refs *9*−*14*), revealing a variety of tertiary contacts that give these molecules their intricate shapes. The discovery of catalytic RNA (*15, 16*) stimulated investigations of how RNA structure allows these molecules to accelerate chemical reactions (*17*). More recently, higher-order RNA structure has been shown to be intimately related to regulation of viral replication (*18*), to expression of alternative protein sequences via programmed frameshifting (*19*−*21*), to suppression of stop codons (*22, 23*), and to translational repression of ribosomal and other proteins (*24*−*26*). However, the energetic rules by which RNA adopts well-defined tertiary structure, and thus can participate in these biologically important functions, are only beginning to be explored systematically (*27*).

RNA folding pathways are also poorly understood. A main feature of the folding of many large, multidomain RNAs is the presence of kinetic traps (*28*−*31*), in which slow (seconds to minutes) unfolding of a misfolded region is the rate-limiting step in the overall folding pathway. Folding of individual RNA domains is even less explored, partly due to a lack of experimental methods useful for monitoring more rapid folding kinetics. The tertiary folding of individual RNA domains is a key link between formation of relatively simple RNA secondary structure elements and the more complex folding pathways of multidomain RNAs.

The 160-nucleotide P4−P6 domain of the *Tetrahymena* group I intron RNA is the first higher-order structure formed during assembly of the catalytically active intron (*32, 33*),

† This work was supported by Grant GM28039 from the National Institutes of Health to T.R.C., Grant GM60819 from the NIH to S.A.W., and Grant 9801382 from the National Science Foundation to S.A.S. S.K.S. was supported by an American Cancer Society postdoctoral fellowship and was a fellow of the Helen Hay Whitney Foundation. T.R.C. is an American Cancer Society Professor. We thank the W. M. Keck foundation for generous support of the Program in Molecular and Cellular Structure on the Boulder campus.

* Correspondence may be addressed to either author. Address for T.R.C.: Department of Chemistry and Biochemistry, Campus Box 215, University of Colorado at Boulder, Boulder, CO 80309-0215; phone (303) 492-8606; fax (303) 492-6194. Present address for S.K.S.: Department of Chemistry, 140 Roger Adams Laboratory, Box 57-5, University of Illinois at Urbana-Champaign, Urbana, IL 61801; phone (217) 244-4489; fax (217) 244-8024; e-mail scott@scs.uiuc.edu.

‡ University of Colorado at Boulder.

§ Johns Hopkins University.

|| Dharmacon Research, Inc.

⊥ Howard Hughes Medical Institute.

[1] Abbreviations: P4−P6, the P4−P6 domain of the *Tetrahymena* group I intron RNA; PAGE, polyacrylamide gel electrophoresis; Tris, tris(hydroxymethyl)aminomethane; TB, Tris−borate buffer; cac, cacodylate; EDTA, ethylenediaminetetraacetic acid; CE, cacodylate−ethylenediaminetetraacetic acid buffer.

10.1021/bi000828y CCC: $19.00
Published on Web 09/14/2000

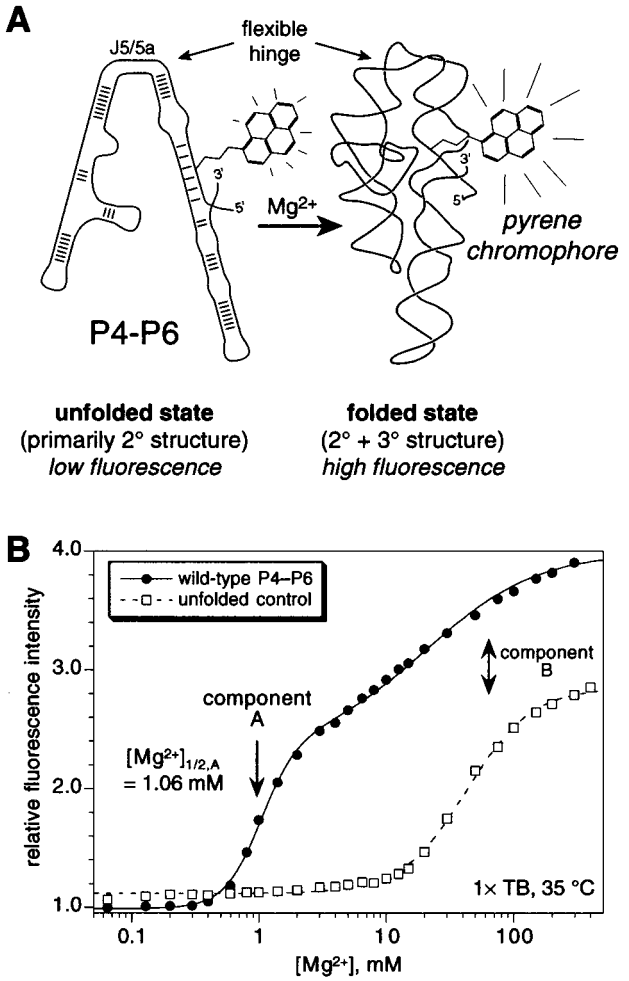

FIGURE 1: Mg^{2+}-dependent tertiary folding and equilibrium fluorescence titrations of pyrene-labeled P4−P6 RNA. (A) Schematic diagram of the tertiary folding of pyrene-labeled P4−P6. In the absence of Mg^{2+}, P4−P6 has secondary structure but little if any tertiary structure, and the fluorescence emission intensity of the covalently attached pyrene is low. Addition of Mg^{2+} induces tertiary folding, and the pyrene fluorescence emission intensity increases (*36*). (B) Equilibrium fluorescence titrations with Mg^{2+} of wild-type P4−P6 [P4−P6-wt-U107(pyr3)] and the unfolded control molecule P4−P6-bp [P4−P6-bp-U107(pyr3)], which is P4−P6 with several base substitutions in the J5/5a "hinge" region that establish Watson−Crick base pairing and thus lock the molecule into an unfolded conformation (*34*). The buffer was the standard Tris−borate buffer 1× TB (89 mM each Tris and boric acid, pH 8.3). Titrations were performed at 35 °C essentially as described (*36*) (see Materials and Methods). All data were fit as described (*36*). For wild-type pyrene-labeled P4−P6, the value of $[Mg^{2+}]_{1/2}$ for component A was 1.06 ± 0.02 mM (n = 3 determinations; error = SEM), and the Mg^{2+} Hill coefficient n was 3.0 ± 0.3.

and it folds independently of the remainder of the intron (*11*, *34*). Folding starts with a well-characterized RNA secondary structure that folds in half at an internal loop (*34*, *35*), forming the two major tertiary interactions observed by X-ray crystallography (Figure 1A) (*11*). Recently we described the use of a fluorescent probe to monitor tertiary folding of this RNA domain (*36*). A pyrene chromophore is covalently tethered to a specific 2′-position in P4−P6; when Mg^{2+} is added to the RNA, the pyrene fluorescence emission intensity increases (Figure 1A). We established that the major component of this fluorescence change is due to tertiary folding of the RNA, although the precise physical explanation for the fluorescence increase is not yet known (*36*). These previous experiments mainly involved equilibrium titrations of the RNA with Mg^{2+}, and only a preliminary determination of the folding kinetics was obtained.

Here we describe stopped-flow fluorescence experiments that monitor the kinetics of Mg^{2+}-induced P4−P6 tertiary folding with millisecond resolution. A key technical advance is the synthesis of a new phosphoramidite **4** that allows preparation of large amounts of pyrene-labeled RNA. Several experiments then permit us to quantify features of the P4−P6 tertiary folding pathway. Under certain conditions, we observe two kinetic phases of folding, revealing the existence of multiple salt- and temperature-dependent P4−P6 folding pathways. We find an excellent correlation between folding kinetics monitored by fluorescence emission and by changes in the hydroxyl radical footprinting pattern (*37*), supporting the validity of both methods in monitoring RNA tertiary structure formation.

MATERIALS AND METHODS

RNA Preparation. Wild-type P4−P6 was labeled with pyrene on a 2′-amino group at nucleotide U107; the resulting RNA is denoted as P4−P6-wt-U107(pyr3) (*36*). RNA was prepared by a modification of the previously described splint ligation strategy (*36*, *38*). The pyr3-labeled 15-mer oligonucleotide representing P4−P6 nucleotides 102−116 was prepared by 5′-silyl-2′-orthoester solid-phase RNA synthesis chemistry (*39*), using the new phosphoramidite **4** described below to incorporate a U(pyr3) residue. The phosphoramidite **4** was dissolved to a concentration of 0.07 M in acetonitrile; with 0.2 M *S*-ethyltetrazole as the activator, **4** coupled in >99% yield within 60 s (data not shown). A T7 RNA polymerase transcript comprising the remaining nucleotides (117−261) of P4−P6 (Δ15-P4−P6 transcript) was prepared as described (*36*). The ligation reaction to join the pyr3-labeled 15-mer oligonucleotide and Δ15-P4−P6 transcript was performed on the 4 nmol scale. Typically four such ligation reactions were pooled before PAGE purification (see strategy 1 in ref *38*), affording approximately 8 nmol of pyrene-labeled P4−P6 per synthesis. Unfolded control RNA with the J5/5a base-pairing substitutions that prevent tertiary folding of P4−P6 [P4−P6-bp-U107(pyr3) (*36*)] was prepared from a Δ15-P4−P6 transcript that was prepared from a mutated DNA template (*34*).

Synthesis of Phosphoramidite **4**. The phosphoramidite **4** was synthesized in three steps from 2′-amino-2′-deoxyuridine **1** (Scheme 1), itself prepared in three steps from uridine according to reported procedures (*40*, *41*). The LiF/TMS−N_3 method (*40*) was used to prepare the 2′-azido-2′-deoxyuridine intermediate.

2′-[(1-Pyrenyl)-4-butyrylamido]-2′-deoxyuridine (**2**). To a mixture of 1.72 g (7.07 mmol) of 2′-amino-2′-deoxyuridine **1** and 3.0 g (7.8 mmol, 1.1 equiv) of **pyr3-NHS** (1-pyrenebutyric acid *N*-hydroxysuccinimide ester, Aldrich) was added 50 mL of anhydrous DMF. The resulting solution was stirred at room temperature under argon for 13 h, and most of the DMF was removed under vacuum. The residue was not sufficiently soluble in neat methanol or CH_2Cl_2 (or a mixture thereof) for silica gel chromatography, so the DMF-containing residue was diluted severalfold with CH_2Cl_2 and quickly loaded onto a silica gel column (230−400 mesh; 4

Scheme 1

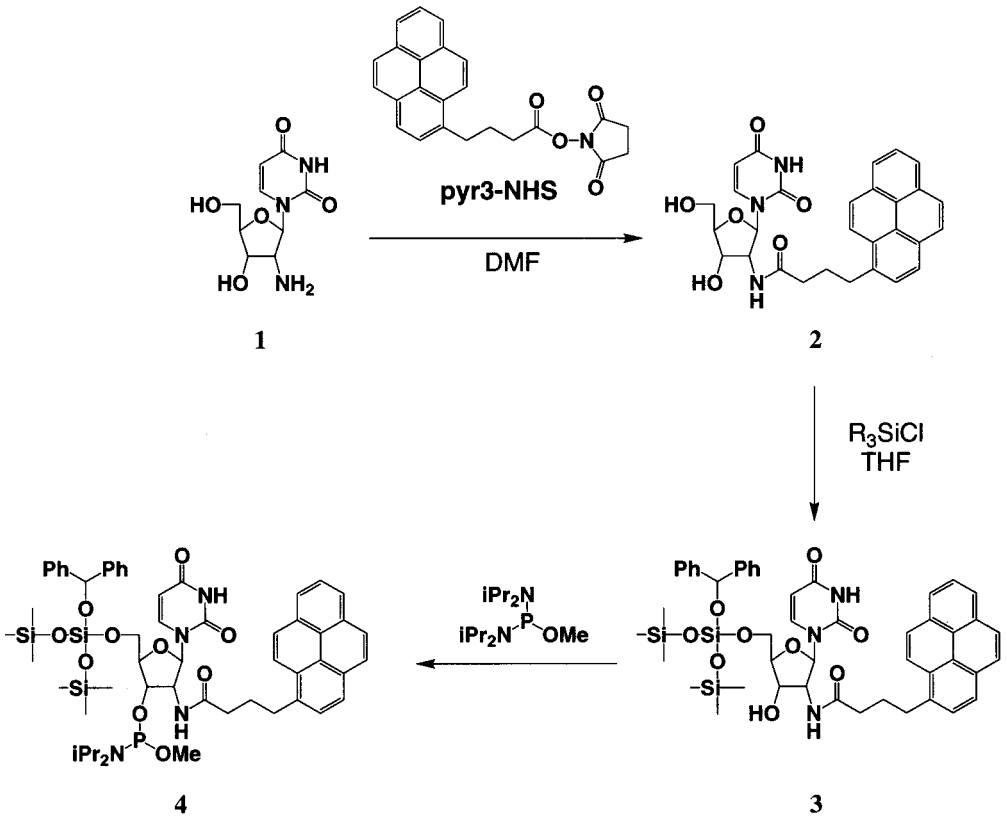

cm diameter, 20 cm height) before precipitation could occur. The column was eluted with ~700 mL of CH_2Cl_2 (the column cracked substantially) and then a gradient to 10% methanol/CH_2Cl_2 until all of the product **2** was eluted. The appropriate fractions were combined and evaporated to afford 2.21 g (61%) of **2** as an off-white solid. ^{1}H NMR (300 MHz, DMSO-d_6) δ 11.24 (s, 1H, uridine NH), 8.34−7.85 (m, 11H, 9 pyrene CH + uridine H-6 + 2′-NH), 5.94 (d, J = 8.5 Hz, 1H, C1′-H), 5.70 (m, 2H, uridine H-5 + OH), 5.19 (t, J = 4.9 Hz, 1H, OH), 4.58 (m, 1H, C2′-H), 4.09 (t, J = 4.6 Hz, 1H, C3′-H or C4′-H), 3.93 (s, 1H, C3′-H or C4′-H), 3.59 (m, 2H, C5′-H_{ab}), 3.22 [t, J = 7.5 Hz, 2H, C(O)CH_2], 2.31 and 1.93 [each m, 2H, C(O)CCH_2CH_2]. FAB-MS $M^{+\bullet}$ 513, $[M + H]^+$ 514. Exact mass HRMS calcd for $C_{29}H_{27}N_3O_6$, 513.1900; found, 513.1920.

5′-O-Bis(trimethylsiloxy)benzhydroxysilyl-2′-[(1-pyrenyl)-4-butyrylamido]-2′-deoxyuridine (**3**). A solution of 2.20 g of **2** (4.28 mmol) in 50 mL of THF containing 0.60 mL of diisopropylamine (4.28 mmol) was stirred at 0 °C. Separately, 9.09 g of bis(trimethylsiloxy)benzhydroxysilyl chloride (BzH-Cl, Dharmacon Research; 21.4 mmol, 5 equiv) was diluted with 25 mL of THF. Diisopropylamine (3.60 mL, 25.7 mmol, 6 equiv) was added slowly to the BzH-Cl solution over 1 min. The solution of silylating reagent was added slowly to the solution of **2** in 3-mL aliquots until **2** was completely consumed as monitored by thin-layer chromatography. The solution was washed with 5% sodium bicarbonate and then with saturated sodium chloride; the organic layer was dried over sodium sulfate and filtered. The product **3** was purified by silica gel chromatography, eluting with a hexanes/ethyl acetate gradient containing 20% acetone, affording 2.97 g (77%) of a clear, colorless oil that was carried directly to the next step.

5′-O-Bis(trimethylsiloxy)benzhydroxysilyl-3′-(P-diisopropylamino-P-methoxy)phosphino-2′-[(1-pyrenyl)-4-butyrylamido]-2′-deoxyuridine (**4**). To a solution of 2.97 g of **3** (3.29 mmol) in 20 mL of CH_2Cl_2 was added 1.29 g of bis(*N*,*N*-diisopropylamino)methoxyphosphine (Dharmacon Research; 4.93 mmol, 1.5 equiv), followed immediately by 0.184 g of tetrazole (2.63 mmol, 0.8 equiv). The solution was stirred at room temperature for 14 h and washed with 5% sodium bicarbonate and then with saturated sodium chloride. The organic layer was dried over sodium sulfate and filtered. The phosphoramidite **4** was purified by silica gel chromatography, eluting with 6:3:1 hexanes/CH_2Cl_2/triethylamine, providing 2.82 g (89%) of a clear, colorless oil. ^{1}H NMR (500 MHz, DMSO-d_6; all assignments based in part on a ^{1}H−^{1}H COSY spectrum) δ 11.38 (s, 1H, uridine NH), 8.34 (dd, 1H) and 8.24 (dd, 2H) and 8.19 (dd, 1H) and 8.14 (dd, 2H) and 8.11 (d, 1H) and 8.04 (t, 1H) and 7.89 (td, 1H) (9H total, pyrene CHs), 7.88 (d, J = 7.5 Hz, 1H, 2′-NH), 7.64 (m, 1H, uridine H-6), 7.39 (d, J = 7.3 Hz, 4H, C2-H of phenyls), 7.28 (t, J = 7.6 Hz, 4H, C3-H of phenyls), 7.19 (tm, J = 7.3 Hz, 2H, C4-H of phenyls), 6.01 (s, 1H, $OCHPh_2$), 5.95 (t, $J_{HCCCOP} \approx J_{C1'\text{-}H-C2'\text{-}H} \approx$ 8.3 Hz, 1H, C1′-H), 5.35 (m, 1H, uridine H-5), 4.72 (dtd, J_{HCCOP} = 37 Hz, $J_{C1'\text{-}H-C2'\text{-}H} \approx J_{C2'\text{-}H-C2'\text{-}NH} \approx$ 8.5 Hz, $J_{C2'\text{-}H-C3'\text{-}H} \approx$ 6.1 Hz, 1H, C2′-H), 4.28 (ddd, J_{HCOP} = 104 Hz, $J_{C3'\text{-}H-C4'\text{-}H}$ = 11.0 Hz, $J_{C2'\text{-}H-C3'\text{-}H}$ = 5.8 Hz, 1H, C3′-H), 4.10 (dm, J_{HCCOP} = 53 Hz, 1H, C4′-H), 3.82 (ddd, J_{HCCCOP} = 17.2 Hz, $J_{C5'\text{-}Ha-C5'\text{-}Hb}$ = 11.5 Hz, $J_{C5'\text{-}Ha-C4'\text{-}H}$ = 3.4 Hz, 1H, C5′-H_a), 3.71 (m, 1H, C5′-H_b), 3.49 (m, 2H, two NC*H*iPr_2), 3.28 [m, 2H, C(O)CH_2], 3.25 and 3.22 ($\Delta\nu$ = 13.2 Hz; each d, J_{HCOP} = 44 Hz, 3H total; overlap with δ 3.28 prevents accurate area ratio determination; $POCH_3$), 2.4−2.2 [m, 2H, C(O)-$CCCH_2$], 2.00 [m, 2H, C(O)CCH_2], 1.04 and 0.98 [$\Delta\nu$ =

26.2 Hz; each dd, total 12H; area ratio ~1.5:1.0; $J = 16.1$ and 6.8 Hz for δ 1.04, 19.1 and 6.8 Hz for δ 0.98; first J_{HCCNP}, second J_{HCCH}; two $NC(CH_3)_2$], 0.01 [m, 9H, $Si(CH_3)_3$], −0.01 [m, 9H, $Si(CH_3)_3$]. The spectrum clearly reflects slow inversion of configuration around P on the NMR time scale at room temperature [two sets of peaks of unequal area for $NC(CH_3)_2$ methyl groups, and two sets of peaks for $POCH_3$]. ESI-MS $[M + H]^+$ 1063, $[M + Na]^+$ 1085, $[M + Et_3N]^+$ 1164.

Equilibrium Fluorescence Titrations. Equilibrium fluorescence measurements were performed on a SLM 48000S spectrometer. The cuvette holder was maintained at 35 °C with a recirculating water bath. Titrations were performed as described (*36*), except that stock solutions of $MgCl_2$ were in 1× concentration of the appropriate buffer instead of water.

Stopped-Flow Fluorescence Measurements. Stopped-flow data were acquired on an Applied Photophysics model 17MV stopped-flow apparatus with $\lambda_{exc} = 319$ nm. The emission was filtered with a Schott KV-370 band-pass filter before entering the photomultiplier tube. For each acquisition, 4000 data points were recorded, and 3−8 acquisitions were averaged to provide each final kinetic trace. The instrument dead time was 1.0−1.3 ms in any given experiment. Stopped-flow folding experiments were initiated by rapidly mixing the contents of the two syringes (RNA in buffer and buffer/Mg^{2+}) in a 1:1 volume ratio. The final RNA concentration after mixing was 1−4 μM. The total volume of solution used per acquisition was 125−150 μL; the sample cell volume was 20 μL. Kinetic traces were fit with single or double exponentials as appropriate by using KaleidaGraph version 3.0.2, providing the values of k_{obs} reported in the text. Residuals for curve fits were calculated at each time point as (data − fit); for all shown fits, the residuals appeared to be distributed randomly around zero over the range of the fit. For most experiments, the pyrene-labeled P4−P6 was collected after each stopped-flow experiment, treated with severalfold excess EDTA, and precipitated with NaCl/ethanol to provide ~90% recovery of material. In several tests, various P4−P6 RNAs that were processed through ~15 such experiments showed fit k_{obs} values indistinguishable from those of freshly synthesized samples (data not shown).

Samples for Mg^{2+}-induced folding were typically annealed by first heating to 90 °C for 2 min in the appropriate buffer in the presence of 0.1 mM EDTA, followed by cooling at room temperature for 20 min and then at 25 °C for 5 min before equilibration in the stopped-flow instrument for ~5 min at the required temperature. No corrections were made for the temperature dependence of the pH of Tris solutions. Although samples were not dialyzed against buffer, the contribution of the RNA itself to the $[Na^+]$ is only ~0.6 mM, assuming a 4 μM sample of a 160-nucleotide RNA with all Na^+ counterions. In experiments with 10 mM sodium cacodylate buffer, pH 7.5, the contribution of Na^+ from the NaOH used to adjust the stock solution's pH was taken as 10 mM Na^+ for simplicity, although the precise contribution is somewhat below this value.

Synchrotron Hydroxyl Radical Footprinting. P4−P6 RNA was prepared and 5′-^{32}P-end-labeled as previously described (*42*, *43*). Samples were dissolved in CE buffer (10 mM sodium cacodylate + 0.1 mM EDTA, pH 7.5) with additional NaCl when indicated and then annealed by heating to 95 °C for 1 min and cooling slowly to 42 °C. Folding kinetics were determined by rapidly mixing the RNA with $MgCl_2$ to 10 mM Mg^{2+} and measuring the time-dependent protection from X-ray-generated hydroxyl radical cleavage as previously reported (*37*). Following X-ray exposure, the RNA was precipitated and analyzed by denaturing PAGE as described (*44*).

RESULTS

New Phosphoramidite for Preparing Pyrene-Labeled RNA. The 160-nucleotide P4−P6 RNA was covalently labeled with the pyrene-containing pyr3 moiety on a 2′-amino-2′-deoxyuridine [the U(pyr3) residue] at nucleotide U107. This was originally accomplished (*36*) by a two-step procedure in which a 15-mer oligonucleotide containing a single 2′-amino-2′-deoxyuridine residue was first derivatized with the *N*-hydroxysuccinimide ester **pyr3-NHS** (see Scheme 1) and then ligated to a 145-nucleotide T7 RNA polymerase transcript, generating full-length pyrene-labeled P4−P6. We have now synthesized a phosphoramidite (**4**, Scheme 1) that allows direct solid-phase synthesis of oligonucleotides containing U(pyr3). 2′-Amino-2′-deoxyuridine **1** (available in multigram quantities in three steps from uridine; *40*, *41*) was derivatized with **pyr3-NHS** to provide 2′-[(1-pyrenyl)-4-butyrylamido]-2′-deoxyuridine **2**, which was 5′-silylated to form **3** and 3′-phosphitylated to afford phosphoramidite **4**. Reagent **4** was used in solid-phase synthesis essentially as described (*39*) to prepare micromole-scale amounts of pyrene-labeled oligonucleotides. These were in turn ligated to transcripts composing the remainder of P4−P6, providing several nanomoles of pyrene-labeled P4−P6 RNA.

Establishing the Conditions for Stopped-Flow Fluorescence Kinetics. When increasing amounts of Mg^{2+} were titrated into a solution of pyrene-labeled P4−P6 at equilibrium, two Mg^{2+}-dependent fluorescence components denoted A and B were observed (Figure 1B), as previously reported (*36*). Only component A reflects tertiary folding of the RNA; component B, which occurs at relatively high $[Mg^{2+}]$, is not correlated with tertiary folding and probably represents more local structural changes. These conclusions are supported by numerous lines of evidence (*36*), an important one of which is that the unfolded control molecule P4−P6-bp (which is unable to undergo global tertiary folding due to base-pairing in the J5/5a hinge region) specifically lacks fluorescence component A (Figure 1B).

We sought to perform stopped-flow kinetics experiments at a $[Mg^{2+}]$ at which component A predominates, to avoid complications from component B. At 35 °C in 1× TB buffer (89 mM each Tris and boric acid, pH 8.3), fluorescence component A of P4−P6 folding is observed with $[Mg^{2+}]_{1/2,A} = 1.06$ mM (Figure 1B). This is slightly higher than the $[Mg^{2+}]_{1/2}$ value of ~0.7 mM at 25 °C (*36*). At 10 times the $[Mg^{2+}]_{1/2}$ value at 35 °C, or 10.6 mM Mg^{2+}, component A appears to be largely complete, while component B has barely begun (Figure 1B). That this $[Mg^{2+}]$ is appropriate for monitoring P4−P6 tertiary folding is strongly supported by the Mg^{2+} titration of unfolded control RNA P4−P6-bp (*34*), for which the change in relative fluorescence intensity at 10.6 mM Mg^{2+} is minimal. Therefore, in our initial stopped-flow experiments with pyrene-labeled P4−P6, we performed a rapid jump from 0 to 10.6 mM Mg^{2+} in 1× TB

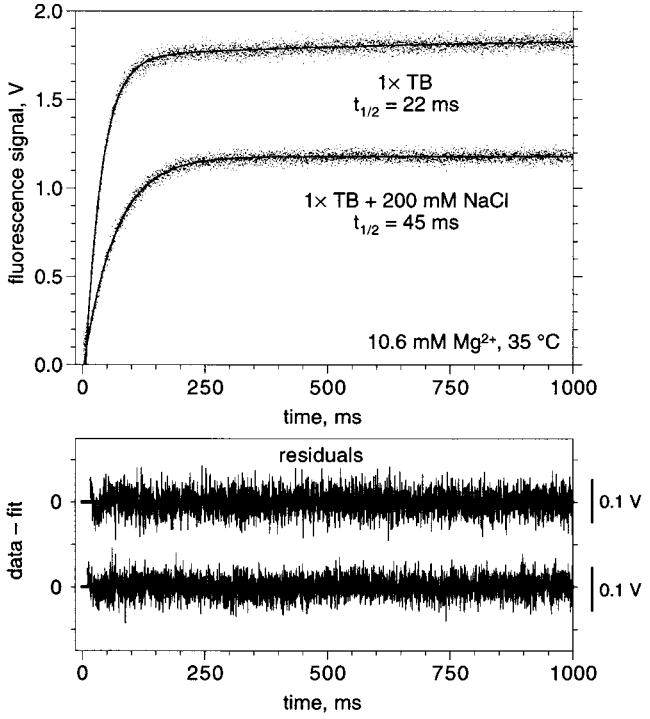

FIGURE 2: Fluorescence kinetics traces for Mg^{2+}-induced folding of pyrene-labeled P4−P6 in Tris−borate buffer in the absence or presence of 200 mM NaCl. Data were collected at 35 °C immediately after 1:1 mixing of ~8 μM pyrene-labeled P4−P6 in buffer (annealed at 90 °C in the presence of 0.1 mM EDTA; see Materials and Methods) with 21.2 mM $MgCl_2$ in buffer, providing final concentrations of ~4 μM RNA and 10.6 mM $MgCl_2$. The instrument dead time was 1.3 ms. For each trace, six acquisitions (each 4000 data points at intervals of 0.25 ms) were averaged. Increasing voltage corresponds to increasing fluorescence intensity. Data were not normalized. The voltage origin for each trace is arbitrary; the traces are vertically offset for clarity. Data from 10 to 1000 ms of the top trace were fit with a double exponential with major (94% of fluorescence change) component $k_{obs} = 31.0 \pm 0.2$ s^{-1} ($t_{1/2} = 22.4 \pm 0.2$ ms) and minor (6%) component $k_{obs} = 1.29 \pm 0.07$ s^{-1} ($t_{1/2} = 0.54 \pm 0.03$ s). Data from 10 to 1000 ms of the bottom trace were fit with a single exponential with $k_{obs} = 15.4 \pm 0.1$ s^{-1} ($t_{1/2} = 45.0 \pm 0.3$ ms). In both cases, additional traces recorded out to 20 s showed no further kinetic components (data not shown).

buffer at 35 °C. Under such conditions, the observed folding rate k_{obs} should have at most a very minor contribution from the unfolding reaction. That is, $k_{obs} = (k_{folding} + k_{unfolding}) \approx k_{folding}$. Note that all three of these k values are composite, not elementary, rate constants, as they encompass both ion binding steps and RNA conformational changes.

Stopped-Flow Fluorescence Experiments Reveal Millisecond Kinetics of P4−P6 Tertiary Folding. Upon mixing pyrene-labeled P4−P6 to a final $[Mg^{2+}] = 10.6$ mM in 1× TB at 35 °C, a substantial fluorescence change on the tens of milliseconds time scale was resolved (Figure 2, upper trace; the instrument dead time was 1.0−1.3 ms in all experiments). These data were best fit by an exponential with major (94%) component $k_{obs} = 31$ s^{-1} ($t_{1/2} = 22$ ms). The minor (6%) component had $k_{obs} = 1.3$ s^{-1} ($t_{1/2} = 540$ ms). Because 1× TB comprises only Tris and boric acid but no added monovalent metal ions, we tested whether the observed kinetics were affected by addition of Na^+. In 1× TB buffer supplemented with 200 mM NaCl, conditions for which the $[Mg^{2+}]_{1/2,A}$ value is shifted to somewhat higher concentration (data not shown), a single exponential with $k_{obs} = 15$ s^{-1} ($t_{1/2} = 45$ ms) provided a satisfactory fit to the fluorescence data (Figure 2, lower trace).

We established that annealing the RNA before folding has little effect on the observed kinetics. In 1× TB, when the RNA samples were not annealed before rapid mixing (data not shown), the kinetic traces and k_{obs} values were essentially equivalent to those observed from samples annealed at 70 °C (data not shown) or at 90 °C (Figure 2).

Comparison of Fluorescence Emission and Synchrotron Hydroxyl Radical Footprinting Kinetics. Kinetics of RNA tertiary folding have also been investigated by hydroxyl radical footprinting (*37*, *45*). In such experiments, hydroxyl radicals generated by exposure of water to X-rays abstract hydrogen atoms from ribose groups, leading to cleavage of the RNA. Residues in the interior of a folded RNA are protected from cleavage (*43*), and the pattern of cleavage and protection provides information about the tertiary structure of the RNA. The kinetics of tertiary folding may be determined by monitoring changes in the extent of cleavage with time.

The folding of the *Tetrahymena* group I intron ribozyme was previously monitored by synchrotron hydroxyl radical footprinting in 10 mM sodium cacodylate buffer, pH 7.5 (*37*); Tris was not used because it scavenges hydroxyl radicals. In these experiments, the P4−P6 domain of the intron was observed to fold at 42 °C with $t_{1/2} \approx 0.7$ s ($k_{obs} \approx 1$ s^{-1}) (*37*). Subsequent experiments on the isolated P4−P6 domain yielded similar results ($t_{1/2} = 0.3$ s, $k_{obs} \approx 2$ s^{-1}; Figure 3; ref *45*). These rates are an order of magnitude slower than those obtained from changes in pyrene fluorescence emission ($t_{1/2} \approx 20-50$ ms in Tris−borate at 35 °C; Figure 2). Either the two techniques monitor different folding transitions, or differences in experimental details (such as ionic strength) give rise to significantly different folding rates.

To compare the fluorescence emission and synchrotron hydroxyl radical footprinting results more directly, we repeated the fluorescence experiments in the same low ionic strength buffer used for the synchrotron experiments (10 mM sodium cacodylate; total $[Na^+] \approx 10$ mM). Under these conditions, a biphasic fluorescence signal was observed at 35 °C upon Mg^{2+}-induced folding of P4−P6 (Figure 4). In contrast, in Tris−borate (which is of moderate ionic strengh even without added Na^+), essentially monophasic kinetics were observed (Figure 2). The sodium cacodylate fluorescence data at 35 °C (Figure 4) were fit with a double exponential, with "fast" and "slow" k_{obs} values of 24 and 0.59 s^{-1} ($t_{1/2} = 29$ ms and 1.2 s). The fast value is similar to that observed in Tris−borate buffer ($t_{1/2} \approx 20-50$ ms; Figure 2), while the slow value is similar to that observed for P4−P6 folding by hydroxyl radical footprinting as described above. The biphasic kinetics suggest that tertiary folding can occur via two different mechanisms in the low ionic strength cacodylate buffer (although a folding intermediate cannot be excluded). The relative amplitudes of the fast and slow kinetic components depended slightly on annealing conditions and on sample history as described in the Figure 4 caption.

It seemed likely that the presence of the slow folding process would depend on ionic strength, because the slow kinetic phase was not observed in Tris−borate, which is of signficantly higher ionic strength than sodium cacodylate.

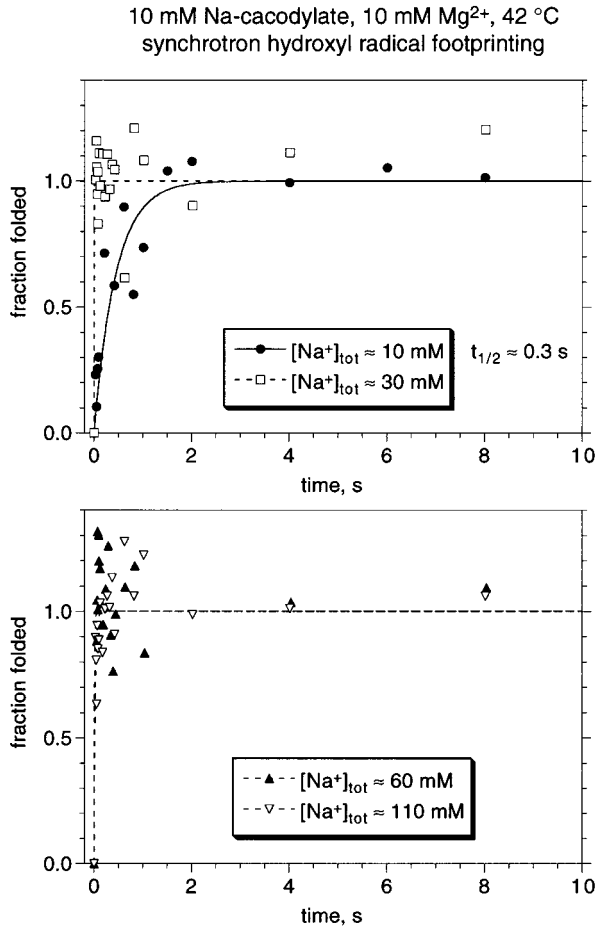

FIGURE 3: Synchrotron hydroxyl radical footprinting kinetics for P4−P6 tertiary folding. 5′-^{32}P-end-labeled P4−P6 RNA (not derivatized with pyrene) was annealed in cacodylate−EDTA (CE) buffer alone (total $[Na^+] \approx 10$ mM; pH 7.5) or in CE supplemented with NaCl to a total Na^+ concentration of 30, 60, or 110 mM (see Materials and Methods). Folding was initiated in a stopped-flow apparatus by mixing to 10 mM Mg^{2+} at 42 °C prior to X-ray exposure (*37*). For each data set, the zero time point was taken from an unfolded control experiment in which P4−P6 was not treated with Mg^{2+} prior to X-ray exposure. Data were normalized and analyzed as described (*37*, *44*). The 10 mM Na^+ data were fit to a single exponential with $t_{1/2} = 0.3 \pm 0.1$ s. The other data were fit to single exponentials with $t_{1/2} \ll 0.1$ s. The instrument dead time is approximately 30 ms.

We therefore examined the fluorescence kinetics in cacodylate buffers containing additional NaCl. At 35 °C, upon increasing $[Na^+]$ to a total of ∼50 mM, the fast fluorescence component remained, but the slow component vanished (Figure 4). These fluorescence results predicted that the slow kinetic component should disappear in the synchrotron hydroxyl radical footprinting experiments when the cacodylate buffer is supplemented with NaCl to increase the ionic strength. As shown in Figure 3, when even small amounts of additional NaCl (∼30 mM total Na^+) were included with cacodylate, tertiary folding of the P4−P6 domain was indeed complete within the dead time of the synchrotron experiment (∼30 ms), consistent with the kinetics observed by fluorescence emission (Figure 4).

Temperature Dependence of P4−P6 Folding Reveals Large Positive Activation Enthalpy and Entropy. To determine the activation enthalpy and entropy parameters $\Delta H^‡$ and $\Delta S^‡$ for P4−P6 tertiary folding, we studied the temperature dependence of the folding kinetics. In Tris−borate−NaCl buffer, the observed folding rate was strongly dependent on temperature between 4 and 45 °C (Figure 5). In particular, the rate at 35 °C ($t_{1/2} = 45$ ms) dropped 3-fold upon lowering the temperature to 25 °C ($t_{1/2} = 147$ ms), another 4−5-fold on cooling to 15 °C ($t_{1/2} = 700$ ms), and another 6-fold at 4 °C ($t_{1/2} = 4.5$ s). The activation parameters calculated from the Eyring plot (circles and solid line in Figure 6) were $\Delta H^‡ = 26$ kcal/mol and $\Delta S^‡ = +31$ eu. The quantitative value of $\Delta S^‡$ depends on the preexponential term in the Eyring equation relating k_{obs} and the activation free energy $\Delta G^‡$, as described elsewhere (S. K. Silverman and T. R. Cech, submitted for publication). In contrast, the value of $\Delta H^‡$ is largely unaffected by the preexponential term. The data above ∼30−35 °C showed apparent non-Arrhenius behavior (Figure 6) and were not used in the analysis.

Temperature-Dependent Switch between Two Kinetics Phases in Low-Salt Cacodylate Buffer. We also examined the temperature dependence of the fluorescence folding kinetics in the low ionic strength sodium cacodylate buffer. Surprisingly, the folding kinetics switched completely from "fast" to "slow" over an extremely narrow temperature range (Figure 7). At 30 °C, the observed kinetics were monophasic and fast, while at 40 °C only the slow phase was detected. Eyring plots for the two phases were obtained (Figure 6) and compared to that for the only (fast) phase observed in Tris−borate buffer. For the fast phase in sodium cacodylate (4−30 °C), the activation parameters ($\Delta H^‡ = 29$ kcal/mol, $\Delta S^‡ = +42$ eu; triangles in Figure 6) were very similar to those observed in Tris−borate, strongly suggesting that the two fast phases represent the same physical process. For the slow phase in sodium cacodylate (32.5−45.0 °C), the activation parameters were significantly larger, $\Delta H^‡ = 44$ kcal/mol and $\Delta S^‡ = +81$ eu (squares in Figure 6).

DISCUSSION

Multiple Salt- and Temperature-Dependent Folding Pathways for P4−P6. In Tris−borate buffer, the rate-determining step in Mg^{2+}-induced tertiary folding of P4−P6 occurs with $k_{obs} = 15-31$ s^{-1} ($t_{1/2} \approx 20-50$ ms) at 35 °C and $[Mg^{2+}] = 10.6$ mM (Figure 2). The precise value of k_{obs} was only slightly (less than 2-fold) affected by inclusion of 200 mM Na^+ (Figure 2), indicating that monovalent metal ions do not play a controlling role in P4−P6 tertiary folding. However, in particularly low ionic strength conditions (10 mM sodium cacodylate buffer; Figure 4), a significant fraction of P4−P6 tertiary folding is rate-limited by a process that occurs much more slowly ($t_{1/2} \approx 1$ s) than does folding in higher ionic strength conditions ($t_{1/2} \approx 20-50$ ms; Figure 2). Increasing the ionic strength by raising the Na^+ concentration (Figure 4) leads to disappearance of the slow folding component. Synchrotron hydroxyl radical footprinting experiments in cacodylate buffer with increased $[Na^+]$ (Figure 3) confirm that the previously reported (*37*) slow kinetics of P4−P6 folding are found only in especially low ionic strength conditions. Such close agreement between two significantly different physical techniques, fluorescence emission and synchrotron hydroxyl radical footprinting, lends confidence that both methods report formation of the native tertiary structure of the P4−P6 RNA domain under a variety of conditions. Our kinetic data for P4−P6 tertiary folding may be summarized as shown in Figure 8, which emphasizes

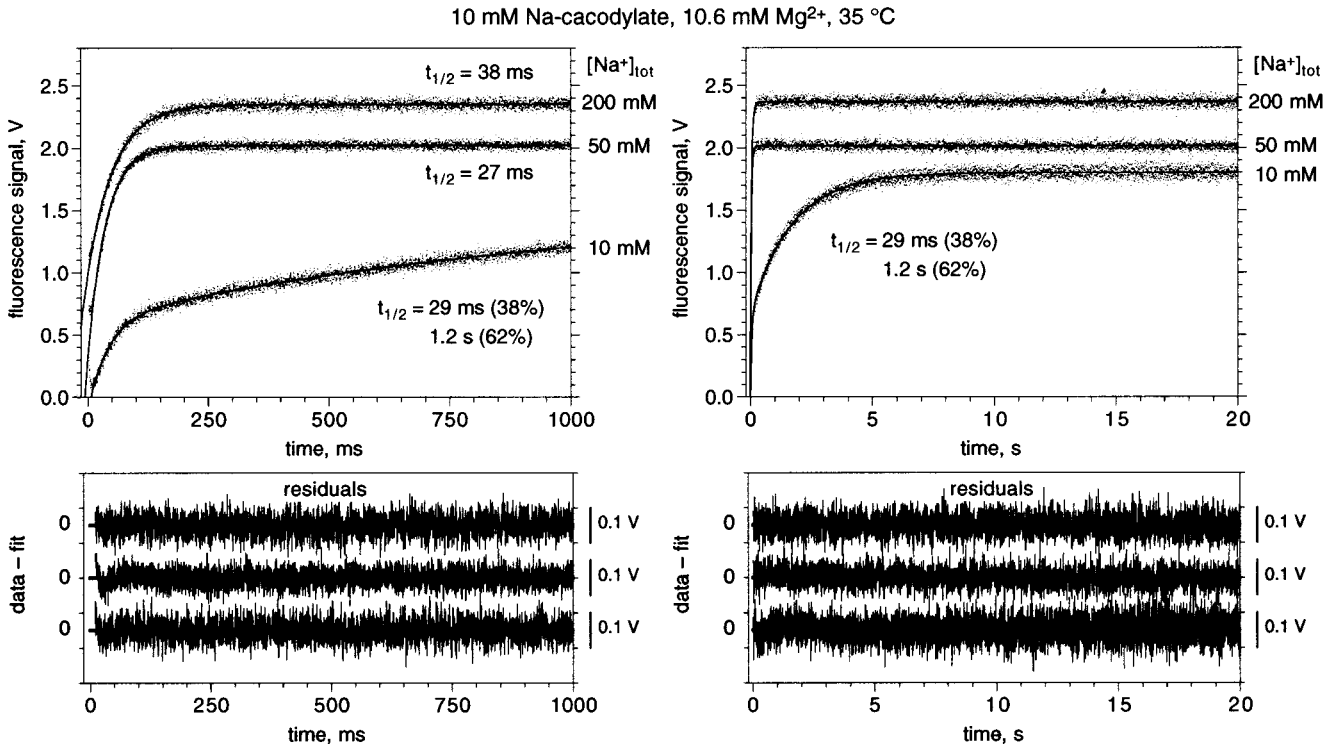

FIGURE 4: Mg^{2+}-induced folding of pyrene-labeled P4−P6 in sodium cacodylate buffer with varying $[Na^+]$. Data were collected as described in the Figure 2 caption. Three experiments are shown, in 10 mM sodium cacodylate buffer supplemented with NaCl to total $[Na^+]$ of 10, 50, or 200 mM (i.e., 10 mM sodium cacodylate + 0, 40, or 190 mM NaCl). For each buffer, the left panel shows a kinetic trace obtained from 0 to 1000 ms after mixing, and the right panel shows data obtained from 0 to 20 s for the same sample. The voltage origin for each trace is arbitrary; the traces are vertically offset for clarity. Data at the lowest $[Na^+]$ were fit with a double exponential with fast component (38% of fluorescence change) $k_{obs} = 24.0 \pm 0.2\ s^{-1}$ ($t_{1/2} = 28.9 \pm 0.2$ ms) [taken from left-panel data, 10−1000 ms] and slow component (62% of fluorescence change) $k_{obs} = 0.585 \pm 0.004\ s^{-1}$ ($t_{1/2} = 1.18 \pm 0.01$ s) [taken from right-panel data, 10 ms−20 s]. The ratio of components was 62% slow/38% fast for the illustrated data, but this varied somewhat depending on annealing conditions (38% slow for an unannealed sample) and on sample history (74% slow for a sample tested after processing through the stopped-flow experiment 18 times as described under Materials and Methods). In all such cases, however, the k_{obs} values were unchanged. Data at higher $[Na^+]$ were fit with single exponentials.

that the slow folding component is observed only at particularly low ionic strength (sodium cacodylate but not Tris−borate) and at higher temperature.

Mechanistic Explanations for the Multiple Folding Pathways. The fast kinetic phase nevertheless has a substantial activation barrier, the possible origins of which are discussed elsewhere (S. K. Silverman and T. R. Cech, submitted for publication). In contrast, the mechanistic explanation for the slow, low ionic strength folding kinetics is unclear. That the kinetics switch completely from fast to slow over a very narrow temperature range (between 30 and 40 °C; Figure 7) implies melting of some structural element that may be either secondary or tertiary in nature. The activation enthalpy $\Delta H^{\ddagger}$ for the slow phase in sodium cacodylate is much larger than $\Delta H^{\ddagger}$ for the fast phase (Figure 6), as might be expected if the slow phase involves secondary structure changes. Although the $t_{1/2} \approx 1$ s is slower than formation of typical RNA secondary structure, rearrangements of secondary structure can occur on the seconds time scale even in buffers of higher ionic strength (*47*), and incorrect secondary structures are known to form in tRNAs under low ionic strength conditions (*48*). However, it is implausible on thermodynamic grounds that the P4−P6 folding kinetics are explained by an aberrant low ionic strength secondary structure. If this were so, then increasing the temperature should favor fast folding as the incorrect secondary structure is melted, whereas only slow folding is observed at higher temperature (Figure 7). A different model postulates that some native P4−P6 secondary structure element is formed poorly in low ionic strength conditions or melted at higher temperature, leading to slow folding via a kinetic trap. While this cannot be ruled out, we consider it unlikely because there is no obvious candidate for such a weak secondary structure element and no independent evidence for a kinetic trap (45).

This prompts us to consider the involvement of tertiary interactions. Although the structure of the initial P4−P6 RNA (in the absence of Mg^{2+}) is not understood at the same level of detail as the crystallographically determined folded structure (*11*), P4−P6 probably has some tertiary interactions in its initial state before Mg^{2+}-induced folding (45). We propose that a subset of initial-state tertiary contacts biases P4−P6 toward formation of its native structure upon addition of Mg^{2+}. In this model, in the low ionic strength sodium cacodylate buffer at lower temperature, such interactions aid relatively fast folding ($t_{1/2} \approx 20-50$ ms). Upon raising the temperature, the initial-state tertiary interactions are disrupted (with melting temperature between 30 and 40 °C), and Mg^{2+}-induced folding is much slower ($t_{1/2} \approx 1$ s; Figure 8). In contrast, in higher ionic strength Tris−borate buffers, these tertiary interactions are not yet melted at the highest temperature examined (45 °C), and only the fast folding is observed.

Two technical concerns may be raised with the fluorescence experiments. One worry is that the some kinetically

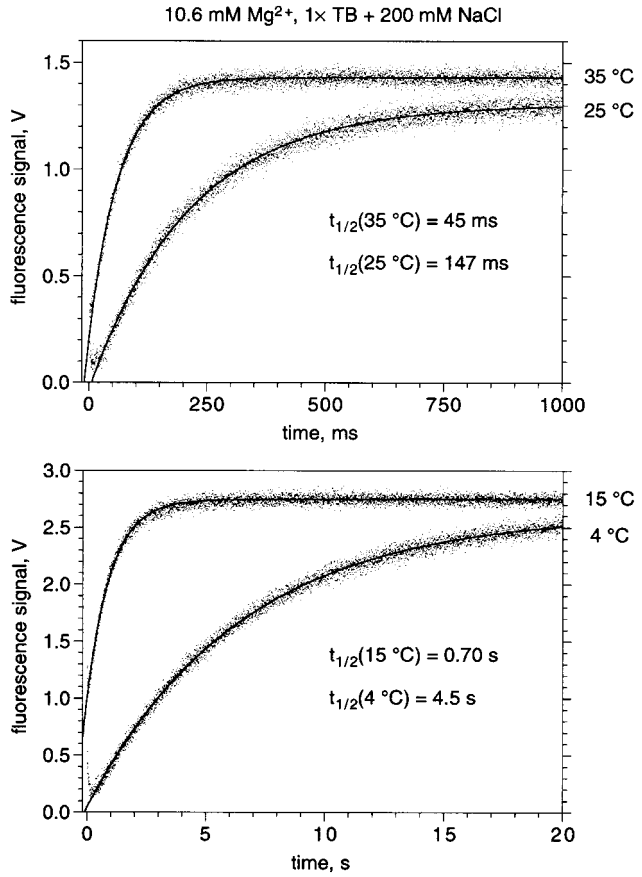

FIGURE 5: Temperature dependence of Mg^{2+}-induced folding of pyrene-labeled P4−P6 in Tris−borate buffer + 200 mM NaCl. Data were obtained between 4 and 35 °C as described in the Figure 2 caption. Note the time scale change between the top (35 and 25 °C) and bottom (15 and 4 °C) panels. The voltage origin for each trace is arbitrary; the traces are vertically offset for clarity. The data at 35, 25, 15, and 4 °C were fit with a single exponential between 10, 10, 25, and 120 ms, respectively, through the end of the displayed trace. The fit values of k_{obs} were 15.4 ± 0.1 s^{-1}, 4.7 ± 0.1 s^{-1}, 0.990 ± 0.004 s^{-1}, and 0.155 ± 0.001 s^{-1}, respectively. Residuals (not shown) were comparable to those shown in Figure 2.

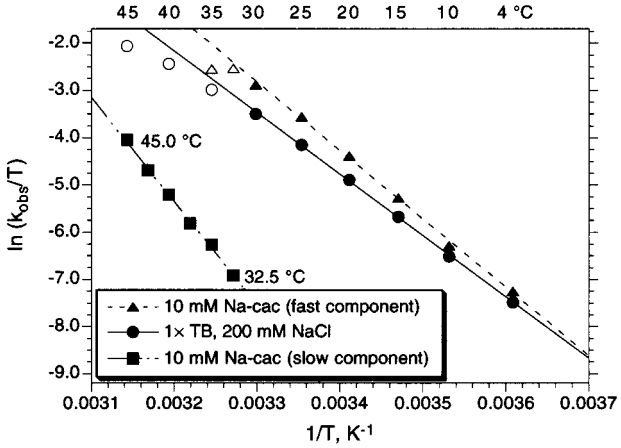

FIGURE 6: Eyring plots for the Mg^{2+}-induced folding of pyrene-labeled P4−P6. In all cases, the final $[Mg^{2+}]$ after mixing was 10.6 mM. For the standard Tris−borate buffer 1× TB + 200 mM NaCl (circles), data were collected as described in the Figure 2 caption. For 10 mM sodium cacodylate buffer, pH 7.5, data were collected as described in the Figures 2 and 4 captions; data for both the fast (triangles) and slow (squares) kinetic components of the fluorescence change are shown. Only the solid symbols were fit with straight lines. To compute the *y*-values, ln (k_{obs}/T), k_{obs} was in reciprocal seconds and temperature T was in kelvins. Because the $[Mg^{2+}]_{1/2}$ value in the Tris−borate−200 mM NaCl buffer is ∼10 mM at 4 °C (data not shown), k_{obs} at this temperature should contain approximately equal contributions from $k_{folding}$ and $k_{unfolding}$. At higher temperature, $k_{obs} \approx k_{folding}$. See text for activation parameters calculated from the fit lines.

relevant part of the folding process causes a negligible change in fluorescence and thus goes undetected. While it is difficult to disprove this rigorously, our data show no evidence of any such missing component. In particular, the absolute amplitude of fluorescence change is similar even when comparing P4−P6 folding under conditions for which the kinetics are dramatically different (Figures 6 and 7), implying that no significant kinetic component of folding is missing. A second concern is that the observed temperature-dependent "switch" between slow and fast kinetics could be explained by a failure to detect the slow kinetic phase at lower temperature because the time scale is too slow; similarly, the fast phase could be too fast to observe at higher temperature. However, we are confident that the kinetic phases not observed at certain temperatures are truly absent, rather than simply too slow or fast to measure, for the following reasons. From the Eyring plot in Figure 6, at 30 °C in 10 mM sodium cacodylate the expected slow-phase $t_{1/2}$ would be ∼4.1 s, and no such phase is observed (Figure 7). At 20 °C the expected slow-phase $t_{1/2}$ would be ∼50 s, and no such phase is observed in data acquired to 100 s (not shown). Similarly, at 45 °C in 10 mM sodium cacodylate, the expected fast-phase $t_{1/2}$ would be 4 ms, easily observable (but not actually observed) with the ∼1 ms stopped-flow dead time.

Comparing P4−P6 Tertiary Folding Kinetics to Models and to Folding of Other RNAs and Proteins. The observed P4−P6 folding rates may be compared with expectations from quantitative models for folding of biopolymers. Such models typically provide an expected folding time $\tau = \tau_0 N^{\omega}$, where τ_0 is a prefactor that depends on solution viscosity and persistence length, N is the number of monomer units in the polymer, and ω depends on the particular folding model (*49*). For the nonspecific collapse of a protein, ω = 2.0−2.2, whereas specific collapse to the native conformation is characterized by ω = 3.8−4.2. For P4−P6, taking N = 160 and τ_0 = 1 ns (*49, 50*), τ values of about 25−70 μs and 200 ms−2 s are calculated for nonspecific and specific collapse. The kinetics shown in Figure 2 fall between these extremes. However, τ_0 clearly depends on the chemical nature of the biopolymer, and because most folding models have been developed for proteins, the folding of polyanionic RNA might best be described by significantly different models.

Our P4−P6 tertiary folding kinetics may be also compared with results of previous experiments on RNA and protein folding. RNA secondary structure typically forms on the 10−100 μs time scale (*1, 48, 51*). tRNA tertiary structure can fold and unfold in milliseconds, provided sufficient salt is present (*52, 53*). Tertiary docking of the substrate helix into the group I intron active site requires several hundred milliseconds (*54, 55*). On the slow end, many conformational changes in large RNAs require seconds to minutes (*29, 30, 32, 33, 56*−*59*) and sometimes even hours (*60*), usually due to kinetic traps. Thirumalai and Woodson (*28*) and also Pan

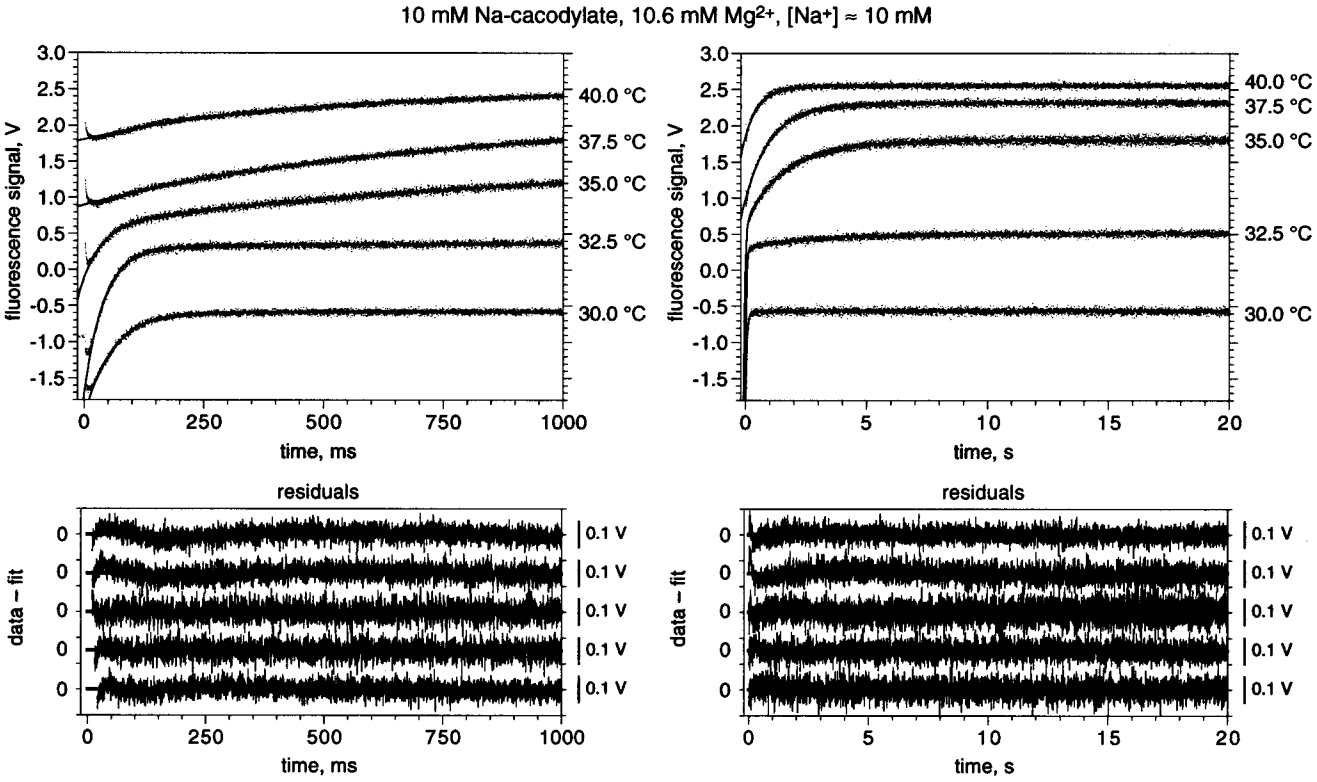

FIGURE 7: Strongly temperature-dependent switch between "fast" and "slow" kinetic phases for Mg^{2+}-induced tertiary folding of P4−P6. Data were obtained between 30.0 and 40.0 °C in 10 mM sodium cacodylate, pH 7.5. The voltage origin for each trace is arbitrary; the traces are vertically offset for clarity. Note that the amplitude of voltage change for each trace is quantitatively similar. The data at 30.0, 37.5, and 40.0 °C were fit with single exponentials, while the data at 32.5 and 35.0 °C were fit with double exponentials. The only (fast) component at 30.0 °C was fit with $k_{obs} = 17.0 \pm 0.1\ s^{-1}$ ($t_{1/2} = 40.8 \pm 0.2$ ms). The kinetic values at 32.5 °C were fast component (92% of fluorescence change) $k_{obs} = 24.2 \pm 0.1\ s^{-1}$ ($t_{1/2} = 28.6 \pm 0.2$ ms) and slow component (8%) $k_{obs} = 0.303 \pm 0.003\ s^{-1}$ ($t_{1/2} = 2.29 \pm 0.02$ s). The data at 35.0 °C are the same as those shown in Figure 4. The only (slow) component at 37.5 °C was fit with $k_{obs} = 0.930 \pm 0.004\ s^{-1}$ ($t_{1/2} = 745 \pm 4$ ms), and at 40.0 °C with $k_{obs} = 1.71 \pm 0.02\ s^{-1}$ ($t_{1/2} = 405 \pm 5$ ms). Double-exponential fits to the 37.5 °C and 40.0 °C data did not improve the residuals (data not shown).

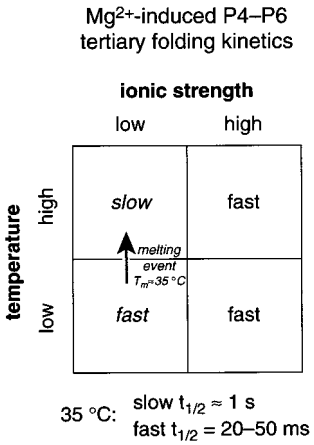

FIGURE 8: Summary of buffer- and temperature-dependent kinetics for Mg^{2+}-induced P4−P6 tertiary folding. The slow folding component is observed only at particularly low ionic strength and higher temperature. In low ionic strength 10 mM sodium cacodylate, the narrow (5−10 °C) temperature range over which the kinetics change from fast to slow (Figure 7) indicates that a melting event is responsible for the kinetics switch. Addition of ~30−50 mM total Na^+ to the cacodylate buffer provides sufficient ionic strength such that the slow component vanishes and folding is entirely fast (Figures 3 and 4). Note that Tris−borate buffer (1× TB) is of sufficient ionic strength even without added Na^+ such that the kinetics are almost entirely monophasic and fast (Figure 2).

and Sosnick (*29*) have suggested that "error-free" RNA folding (i.e., folding not limited by kinetic traps) can occur in milliseconds. Our observation of kinetics on this approximate time scale (Figure 2) suggests that, under appropriate conditions, P4−P6 tertiary folding is an example of such a process.

The activation parameters $\Delta H^{\ddagger}$ and $\Delta S^{\ddagger}$ for P4−P6 tertiary folding may be related to values for other RNAs. One of the best-studied RNA conformational changes is the docking of the P1 (substrate·internal guide sequence) double helix into the catalytic site of the group I intron ribozyme (*55*, *61*). An activation enthalpy $\Delta H^{\ddagger} = 22$ kcal/mol was observed (*55*), close to the $\Delta H^{\ddagger} = 26-29$ kcal/mol observed for P4−P6 tertiary folding in Tris−borate (Figure 6). For P1 docking, this value was interpreted to mean that docking is not diffusion-controlled. Similarly, the substantial activation barrier for P4−P6 tertiary folding has implications for the nature of the folding transition state, as described elsewhere (S. K. Silverman and T. R. Cech, submitted for publication). Even larger $\Delta H^{\ddagger}$ values for RNA tertiary folding processes are known (*59*, *62*). The positive activation entropy $\Delta S^{\ddagger}$ for P4−P6 folding, $\Delta S^{\ddagger} = +31$ eu, is larger than that observed for P1 docking ($\Delta S^{\ddagger} = +21$ eu, both calculated with a $k_B T/h$ Eyring preexponential). In both cases, the positive $\Delta S^{\ddagger}$ may originate in release of Mg^{2+}-coordinated water upon formation of tertiary contacts in the folding transition state, although other explanations are possible (*55*).

Protein folding kinetics also cover a large range of time scales. The "speed limit" for protein folding is ~1 μs (*63*−*66*), and examples of submillisecond protein folding continue

to be identified (*67*, *68*). However, even some proteins that fold by simple two-state transitions do so much more slowly, requiring seconds (*69*, *70*). When kinetic traps are present, protein folding can take even longer (*71*, *72*), similar to RNA. The relationship between protein folding and RNA folding is not entirely clear (but see ref *28*), in part because relatively little information is available about the latter process.

RNA Folding Events at Very Fast Time Scales? We note that in addition to the fluorescence increase upon Mg^{2+}-induced folding, there is an initial *decrease* in fluorescence at very fast time scales (see, for example, the 4 °C trace in Figure 5). Under conditions where the folding reaction is extremely slow, e.g., at lower temperature and [Mg^{2+}], this initial fluorescence decrease can be more clearly observed (data not shown). The rate of the initial decrease is 2−3 orders of magnitude faster than that of the fluorescence increase caused by tertiary folding (data not shown). Under buffer and temperature conditions where the folding $t_{1/2}$ is on the order of tens of milliseconds (Figure 2), this initial event is extrapolated to occur with $t_{1/2}$ on the order of tens to hundreds of microseconds. Although this is far too fast for resolution by conventional stopped-flow experiments, this is the approximate time scale suggested for fundamental dynamical changes in RNA structure (*73*). These observations suggest the need to develop experimental approaches for resolving RNA structural changes on the microsecond time scale. The analogous need for ultrafast measurements of protein folding has also been emphasized recently (*49*, *74*, *75*).

Concluding Remarks. Current theories for protein folding emphasize the "funnel" characteristics of protein folding landscapes, in favor of folding pathways proceeding through well-defined structural intermediates (*28*, *76*−*84*). Energy landscape models also explain many features of RNA folding (*28*), although further kinetic investigations are clearly warranted. Our finding of multiple P4−P6 folding pathways shows that the pathway and kinetics of RNA folding can depend greatly on ionic strength and temperature. We hope that further kinetic measurements such as those presented here will help to clarify the nature of RNA tertiary folding pathways.

ACKNOWLEDGMENT

We thank Susy Kohout for frequent assistance in maintaining the stopped-flow fluorescence spectrometer and David Kitchen for RNA oligonucleotide synthesis.

REFERENCES

1. Crothers, D. M., Cole, P. E., Hilbers, C. W., and Shulman, R. G. (1974) *J. Mol. Biol. 87*, 63−88.
2. Hilbers, C. W., Robillard, G. T., Shulman, R. G., Blake, R. D., Webb, P. K., Fresco, R., and Riesner, D. (1976) *Biochemistry 15*, 1874−1882.
3. Fresco, J. (1998) In *RNA Structure and Function* (Simons, R. W., and Grunberg-Manago, M., Eds.) pp 1−35, Cold Spring Harbor Laboratory Press, Cold Spring Harbor, NY.
4. Kim, S. H., Quigley, G. J., Suddath, F. L., McPherson, A., Sneden, D., Kim, J. J., Weinzierl, J., and Rich, A. (1973) *Science 179*, 285−288.
5. Robertus, J. D., Ladner, J. E., Finch, J. T., Rhodes, D., Brown, R. S., Clark, B. F., and Klug, A. (1974) *Nature 250*, 546−551.
6. Schevitz, R. W., Podjarny, A. D., Krishnamachari, N., Hughes, J. J., Sigler, P. B., and Sussman, J. L. (1979) *Nature 278*, 188−190.
7. Moras, D., Comarmond, M. B., Fischer, J., Weiss, R., Thierry, J. C., Ebel, J. P., and Giege, R. (1980) *Nature 288*, 669−674.
8. Woo, N. H., Roe, B. A., and Rich, A. (1980) *Nature 286*, 346−351.
9. Pley, H. W., Flaherty, K. M., and McKay, D. B. (1994) *Nature 372*, 68−74.
10. Scott, W. G., Finch, J. T., and Klug, A. (1995) *Cell 81*, 991−1002.
11. Cate, J. H., Gooding, A. R., Podell, E., Zhou, K., Golden, B. L., Kundrot, C. E., Cech, T. R., and Doudna, J. A. (1996) *Science 273*, 1678−1685.
12. Ferré-D'Amaré, A. R., Zhou, K., and Doudna, J. A. (1998) *Nature 395*, 567−574.
13. Hoogstraten, C. G., Legault, P., and Pardi, A. (1998) *J. Mol. Biol. 284*, 337−350.
14. Wedekind, J. E., and McKay, D. B. (1999) *Nat. Struct. Biol. 6*, 261−268.
15. Kruger, K., Grabowski, P. J., Zaug, A. J., Sands, J., Gottschling, D. E., and Cech, T. R. (1982) *Cell 31*, 147−157.
16. Guerrier-Takada, C., Gardiner, K., Marsh, T., Pace, N., and Altman, S. (1983) *Cell 35*, 849−857.
17. Cech, T. R., and Herschlag, D. (1996) In *Nucleic Acids and Molecular Biology*, Vol. 10 (Eckstein, F., and Lilley, D. M. J., Eds.) pp 1−17, Springer, Berlin.
18. Olsthoorn, R. C. L., Mertens, S., Brederode, F. T., and Bol, J. F. (1999) *EMBO J. 18*, 4856−4864.
19. Brierley, I., Digard, P., and Inglis, S. C. (1989) *Cell 57*, 537−547.
20. Liphardt, J., Napthine, S., Kontos, H., and Brierley, I. (1999) *J. Mol. Biol. 288*, 321−335.
21. Kim, Y.-G., Su, L., Maas, S., O'Neill, A., and Rich, A. (1999) *Proc. Natl. Acad. Sci. U.S.A. 96*, 14234−14239.
22. Wills, N. M., Gesteland, R. F., and Atkins, J. F. (1991) *Proc. Natl. Acad. Sci. U.S.A. 88*, 6991−6995.
23. Alam, S. L., Wills, N. M., Ingram, J. A., Atkins, J. F., and Gesteland, R. F. (1999) *J. Mol. Biol. 288*, 837−852.
24. Tang, C. K., and Draper, D. E. (1989) *Cell 57*, 531−536.
25. Bénard, L., Philippe, C., Dondon, L., Grunberg-Manago, M., Ehresmann, B., Ehresmann, C., and Portier, C. (1994) *Mol. Microbiol. 14*, 31−40.
26. Kiser, K. B., and Schmidt, M. G. (1999) *Curr. Microbiol. 38*, 113−121.
27. Tinoco, I., Jr., and Bustamante, C. (1999) *J. Mol. Biol. 293*, 271−281.
28. Thirumalai, D., and Woodson, S. A. (1996) *Acc. Chem. Res. 29*, 433−439.
29. Pan, T., and Sosnick, T. R. (1997) *Nat. Struct. Biol. 4*, 931−938.
30. Rook, M. S., Treiber, D. K., and Williamson, J. R. (1998) *J. Mol. Biol. 281*, 609−620.
31. Treiber, D. K., and Williamson, J. R. (1999) *Curr. Opin. Struct. Biol. 9*, 339−345.
32. Zarrinkar, P. P., and Williamson, J. R. (1994) *Science 265*, 918−924.
33. Downs, W. D., and Cech, T. R. (1996) *RNA 2*, 718−732.
34. Murphy, F. L., and Cech, T. R. (1993) *Biochemistry 32*, 5291−5300.
35. Szewczak, A. A., and Cech, T. R. (1997) *RNA 3*, 838−849.
36. Silverman, S. K., and Cech, T. R. (1999) *Biochemistry 38*, 14224−14237.
37. Sclavi, B., Sullivan, M., Chance, M. R., Brenowitz, M., and Woodson, S. A. (1998) *Science 279*, 1940−1943.
38. Silverman, S. K., and Cech, T. R. (1999) *Biochemistry 38*, 8691−8702.
39. Scaringe, S. A., Wincott, F. E., and Caruthers, M. H. (1998) *J. Am. Chem. Soc. 120*, 11820−11821.
40. McGee, D. P. C., Vargeese, C., Zhai, Y., Kirschenheuter, G. P., Settle, A., Siedem, C. R., and Pieken, W. A. (1995) *Nucleosides Nucleotides 14*, 1329−1339.
41. Verheyden, J. P. H., Wagner, D., and Moffatt, J. G. (1971) *J. Org. Chem. 36*, 250−254.

42. Zaug, A. J., Grosshans, C. A., and Cech, T. R. (1988) *Biochemistry 27*, 8924−8931.
43. Latham, J. A., and Cech, T. R. (1989) *Science 245*, 276−282.
44. Sclavi, B., Woodson, S., Sullivan, M., Chance, M. R., and Brenowitz, M. (1997) *J. Mol. Biol. 266*, 144−159.
45. Deras, M. L., Brenowitz, M., Ralston, C. Y., Chance, M. R., and Woodson, S. A. (2000) *Biochemistry*, in press.
46. Deleted in press.
47. LeCuyer, K. A., and Crothers, D. M. (1994) *Proc. Natl. Acad. Sci. U.S.A. 91*, 3373−3377.
48. Cole, P. E., Yang, S. K., and Crothers, D. M. (1972) *Biochemistry 11*, 4358−4368.
49. Thirumulai, D. (1995) *J. Phys. I France 5*, 1457−1467.
50. Pan, J., Thirumalai, D., and Woodson, S. A. (1999) *Proc. Natl. Acad. Sci. U.S.A. 96*, 6149−6154.
51. Draper, D. E. (1996) *Nat. Struct. Biol. 3*, 397−400.
52. Cole, P. E., and Crothers, D. M. (1972) *Biochemistry 11*, 4368−4374.
53. Urbanke, C., Römer, R., and Maass, G. (1975) *Eur. J. Biochem. 55*, 439−444.
54. Bevilacqua, P. C., Kierzek, R., Johnson, K. A., and Turner, D. H. (1992) *Science 258*, 1355−1358.
55. Li, Y., Bevilacqua, P. C., Mathews, D., and Turner, D. H. (1995) *Biochemistry 34*, 14394−14399.
56. Zarrinkar, P. P., Wang, J., and Williamson, J. R. (1996) *RNA 2*, 564−573.
57. Pan, J., Thirumalai, D., and Woodson, S. A. (1997) *J. Mol. Biol. 273*, 7−130.
58. Pan, J., and Woodson, S. A. (1998) *J. Mol. Biol. 280*, 597−609.
59. Fang, X., Pan, T., and Sosnick, T. R. (1999) *Nat. Struct. Biol. 6*, 1091−1095.
60. Gluick, T. C., Gerstner, R. B., and Draper, D. E. (1997) *J. Mol. Biol. 1997*, 451−463.
61. Herschlag, D. (1992) *Biochemistry 31*, 1386−1399.
62. Emerick, V. L., Pan, J., and Woodson, S. A. (1996) *Biochemistry 35*, 13469−13477.
63. Hagen, S. J., Hofrichter, J., Szabo, A., and Eaton, W. A. (1996) *Proc. Natl. Acad. Sci. U.S.A. 93*, 11615−11617.
64. Eaton, W. A., Muñoz, V., Thompson, P. A., Chan, C.-K., and Hofrichter, J. (1997) *Curr. Opin. Struct. Biol. 7*, 10−14.
65. Wittung-Stafshede, P., Lee, J. C., Winkler, J. R., and Gray, H. B. (1999) *Proc. Natl. Acad. Sci. U.S.A. 96*, 6587−6590.
66. Wildegger, G., Liemann, S., and Glockshuber, R. (1999) *Nat. Struct. Biol. 6*, 550−553.
67. Spector, S., and Raleigh, D. P. (1999) *J. Mol. Biol. 293*, 763−768.
68. Park, S.-H., Shastry, M. C. R., and Roder, H. (1999) *Nat. Struct. Biol. 6*, 943−947.
69. Guijarro, J. I., Morton, C. J., Plaxco, K. W., Campbell, I. D., and Dobson, C. M. (1998) *J. Mol. Biol. 276*, 657−667.
70. van Nuland, N. A. J., Chiti, F., Taddei, N., Raugei, G., Ramponi, G., and Dobson, C. M. (1998) *J. Mol. Biol. 283*, 883−891.
71. Fedorov, A. N., and Baldwin, T. O. (1999) *J. Mol. Biol. 294*, 579−586.
72. Bhuyan, A. K., and Udgaonkar, J. B. (1999) *Biochemistry 38*, 9158−9168.
73. Cohen, S. B., and Cech, T. R. (1997) *J. Am. Chem. Soc. 119*, 6259−6268.
74. Roder, H., and Shastry, M. C. R. (1999) *Curr. Opin. Struct. Biol. 9*, 620−626.
75. Brockwell, D. J., Smith, D. A., and Radford, S. E. (2000) *Curr. Opin. Struct. Biol. 10*, 16−25.
76. Leopold, P. E., Montal, M., and Onuchic, J. N. (1992) *Proc. Natl. Acad. Sci. U.S.A. 89*, 8721−8725.
77. Bryngelson, J. D., Onuchic, J. N., Socci, N. D., and Wolynes, P. G. (1995) *Proteins: Struct., Funct., Genet. 21*, 167−195.
78. Onuchic, J. N., Socci, N. D., Luthey-Schulten, Z., and Wolynes, P. G. (1996) *Folding Des. 1*, 441−450.
79. Dill, K. A., and Chan, H. S. (1997) *Nat. Struct. Biol. 4*, 10−19.
80. Lazaridis, T., and Karplus, M. (1997) *Science 278*, 1928−1931.
81. Fersht, A. R. (1997) *Curr. Opin. Struct. Biol. 7*, 3−9.
82. Onuchic, J. N., Luthey-Schulten, Z., and Wolynes, P. G. (1997) *Annu. Rev. Phys. Chem. 48*, 545−600.
83. Socci, N. D., Onuchic, J. N., and Wolynes, P. G. (1998) *Proteins: Struct., Funct., Genet. 32*, 136−158.
84. Dobson, C. M., and Karplus, M. (1999) *Curr. Opin. Struct. Biol. 9*, 92−101.

BI000828Y